

1 Modeling tabular icebergs coupled to an ocean model

2 **A. A. Stern¹, A. Adcroft¹, O. Sergienko¹, G. Marques¹, R. Hallberg¹**

3 ¹Geophysical Fluid Dynamics Laboratory, Princeton University

4 ¹201 Forrestal Rd, Princeton, NJ 08540, USA

5 **Key Points:**

- 6 • = enter point 1 here =
7 • = enter point 2 here =
8 • = enter point 3 here =

9 **Abstract**

10 The calving of giant icebergs from the Antarctic ice shelves accounts for approximately
 11 half of Antarctic ice-shelf decay. After calving, these tabular icebergs drift across large
 12 distances, altering regional ocean circulation, bottom-water formation, sea-ice produc-
 13 tion and biological primary productivity in the icebergs' vicinity. However, despite their
 14 importance, the current generation of numerical models is unable to represent giant tabu-
 15 lar icebergs in a physically realistic way. In this study we develop a novel framework to
 16 model giant tabular icebergs submerged in the ocean. In this framework, tabular icebergs
 17 are constructed out of Lagrangian elements that drift in the ocean, and are held together
 18 by numerical bonds. By breaking these bonds, a tabular iceberg can be made to split into
 19 smaller pieces, or to break away from an ice shelf. We describe the Lagrangian tabular-
 20 iceberg model and discuss a number of the technical elements involved in its development.
 21 We demonstrate the capabilities of the model by modeling a tabular iceberg drifting away
 22 an idealized ice shelf.

23 **1 Introduction**

24 The Antarctic ice shelves are characterized by large infrequent calving events where
 25 massive pieces of the ice shelves break off, to create giant tabular icebergs. Observational
 26 estimates suggest that over the past 30 years approximately half of Antarctic ice-shelf de-
 27 cay is due to iceberg calving, while the other half occurs through ice-shelf melting [De-
 28 poorter et al , 2013; Rignot et al , 2013]. Iceberg sizes appear to fit a power law distri-
 29 bution, with the majority of icebergs being small ($L < 1 \text{ km}$), while the far less numerous
 30 giant tabular icebergs ($L > 5\text{km}$) account for more than 90% of the icebergs mass [Tour-
 31 nadre et al , 2016].

32 After calving, icebergs slowly drift away from their source glaciers, often becom-
 33 ing stuck in sea ice, or grounding along the Antarctic coast [Lichey and Hellmer , 2001;
 34 Dowdeswell and Bamber , 2007]. Giant tabular icebergs extend deep into the water col-
 35 umn, and have the potential to disrupt ocean circulation patterns for months or even years
 36 after calving [Robinson et al , 2012; Stern et al , 2015]. The freshwater flux from iceberg
 37 melt impacts ocean hydrography around the iceberg, influencing sea-ice production and
 38 bottom-water formation [Arrigo et al , 2002; Robinson et al , 2012; Nicholls et al , 2009].
 39 The long distances traveled by giant icebergs before melting means that their meltwater
 40 impact is often felt hundreds of kilometers away from their calving origins [Stern et al ,
 41 2016]. Meltwater injection (and the accompanying upwelling) from icebergs can also in-
 42 fluence biological productivity by providing nutrients to the surface ocean or changing sea
 43 ice conditions [Arrigo et al , 2002; Vernet et al , 2012; Biddle et al , 2015]. The increased
 44 productivity associated with free-floating tabular icebergs has been linked with local in-
 45 creases in ocean carbon uptake, potentially large enough to be a significant fraction of the
 46 Southern Ocean carbon sequestration [Smith et al , 2007].

47 In recent years, there has been an increased interest in iceberg drift and decay. This
 48 surge of interest has been driven by (i) the need to understand polar freshwater cycles
 49 in order to create realistic climate forecasts and sea level projections [Silva et al , 2006;
 50 Shepherd and Wingham , 2007; Rignot et al , 2013]; and (ii) the increased use of high-
 51 latitudes iceberg-filled waters for shipping lanes and offshore hydrocarbon exploration
 52 in the Arctic [Pizzolato et al , 2012; Unger , 2014; Henderson and Loe , 2016]. The in-
 53 creased interest in icebergs has led to the development of numerical models of iceberg
 54 drift and decay [Mountain , 1980; Bigg et al , 1997; Gladstone et al , 2001; Kubat et al
 55 , 2005], some of which have been included in global General Circulation Models [Mar-
 56 tin and Adcroft , 2010; Marsh et al , 2015]. These iceberg drift models treat icebergs as
 57 Lagrangian point particles, which are advected by the flow, and melt according to cer-
 58 tain parameterizations for icebergs melt. Since icebergs are treated as point particles, ice-
 59 berg drift models are mostly suitable for modeling icebergs smaller than an ocean grid

60 cell. Consequently, these models have mostly been used to represent icebergs smaller than
 61 3.5km on a global scale [Jongma et al , 2009; Martin and Adcroft , 2010; Marsh et al ,
 62 2015].

63 Point-particle iceberg drift models are less suitable for modeling larger tabular ice-
 64 bergs, where the size and structure of the iceberg may be an important feature in deter-
 65 mining their drift and decay [Stern et al , 2016]. They also are not suitable for studying
 66 the local effects that icebergs have on the surrounding ocean, or the small scale processes
 67 that influence iceberg melt and decay [Wagner et al , 2014; Stern et al , 2015]. For this
 68 reason, tabular icebergs ($L > 5\text{km}$) are currently not represented in the iceberg drift mod-
 69 els used in climate models, even though observations suggest that tabular icebergs account
 70 for the vast majority of the total Southern Hemisphere iceberg mass [Tournadre et al ,
 71 2016].

72 The goal of this study is to develop a new iceberg model where tabular icebergs are
 73 explicitly resolved. In this model, icebergs are no longer treated as point particles that
 74 interact with the ocean at a single location, but rather icebergs are given structure, so that
 75 they interact with the ocean across multiple ocean grid cells and depress the ocean surface
 76 over a wide area. To do this, we create tabular icebergs out of many Lagrangian elements
 77 with finite extent which are ‘bonded’ together by numerical bonds. The numerical bonds
 78 hold the ice elements together and allow a collection of elements to move as a unit. By
 79 manually breaking these bonds, we can simulate iceberg calving, allowing us to study the
 80 ocean response to giant iceberg detaching from an ice shelf (e.g.: Figure 8 and 8) or the
 81 fracturing of a large iceberg into smaller pieces.

82 The discrete element model (DEM) developed in this study is referred to at the La-
 83 grangian Tabular Iceberg Model (LTIM). Section 2 gives a description of many of the key
 84 aspects of the LTIM. Since this model is a new approach to modeling icebergs, we present
 85 many of the technical elements involved in constructing the model. In section 3 and 4, we
 86 demonstrate the capabilities of the model by simulating a tabular iceberg detaching from
 87 an idealized ice shelf.

88 2 Model description

89 The LTIM is a Lagrangian particle-based model (or DEM model) in that the ob-
 90 jects of the model are Lagrangian elements. Each element represents a mass of ice that is
 91 floating in the ocean, and has a position, velocity, mass, and a set of dimensions, which
 92 can evolve in time. The motion of each element is determined by a momentum equa-
 93 tion which is solved in the (Lagrangian) reference frame of the element. The elements
 94 are forced by oceanic and atmospheric forces, which are provided by the user, or are de-
 95 termined by coupling the LTIM to an ocean/atmosphere model. The elements also inter-
 96 act with one another and can be bonded together to form larger structures. The angular
 97 momentum of the elements is not modeled explicitly; instead rotational motion of larger
 98 structures emerge as a consequence of bond orientation and collective motion. In differ-
 99 ent contexts, the LTIM elements can be thought to represent individual icebergs, sea ice
 100 flows, or, when the elements are bonded together, they can represent larger structures such
 101 as tabular icebergs or ice shelves.

102 The LTIM model is developed on the code base of an existing iceberg drift model
 103 [Martin and Adcroft , 2010; Stern et al , 2016]. When run with the correct set of runtime
 104 flags, the model runs as a traditional iceberg drift model.

105 2.1 Equations of motion

106 The elements drift in the ocean, forced by atmosphere, ocean and sea-ice drag forces,
 107 as well as the Coriolis force and a force due to the sea surface slope. When these ice el-

ements move alone (without interactions with other elements), they can be thought of as representing individual (or clusters of) small icebergs, and follow the same equations described in the iceberg drift model of Martin and Adcroft [2010] (based on the equations outlined in Bigg et al [1997] and Gladstone et al [2001]).

In addition to the environmental forces, the elements in the LTIM model experience interactive forces due to the presence of other elements. Two types of interactive forces are included between elements. The first force is a repulsive force which is applied to elements to prevent them from moving too close to one another. This repulsive force prevents icebergs from piling up on top of one another. The second interactive force is a force due to numerical ‘bonds’, and is only applied if two elements are labelled as ‘bonded’. When two elements are bonded, each element feels an attractive force that prevents the elements from moving too far apart from one another. The interactive forces between two bonded elements are defined such that in the absence of other forces the elements come to rest adjacent to one another, with no overlap of the iceberg areas.

The momentum equation for each element is given by

$$M \frac{D\vec{u}}{Dt} = \vec{F}_A + \vec{F}_W + \vec{F}_R + \vec{F}_C + \vec{F}_{SS} + \vec{F}_{SI} + \vec{F}_{IA}, \quad (1)$$

where $\frac{D}{Dt}$ is the total (Lagrangian) derivative, M is the mass of the element, \vec{u} is the velocity of the element, and the terms on the right hand side give the forces on the element due to air drag (\vec{F}_A), water drag (\vec{F}_W), sea ice drag (\vec{F}_{SI}), Coriolis force (\vec{F}_C), wave radiation force (\vec{F}_R), sea surface slope (\vec{F}_{SS}), and interactions with other elements (\vec{F}_{IA}). The environmental forces are the same as those presented in Martin and Adcroft [2010], and are provided for completeness in Appendix A. The details of the interactive forces are provided in below.

2.2 Interactive Forces

The interactive force on an element is calculated by adding together the interactions with all other elements, such that the interactive force on element i , $(\vec{F}_{IA})_i$ is given by:

$$(\vec{F}_{IA})_i = \sum_{j \neq i} (\vec{F}_{IA})_{ij}, \quad (2)$$

where $(\vec{F}_{IA})_{ij}$ is the force on element i by element j . Both bonded and repulsive interactions are modeled using elastic stresses with frictional damping. The elastic component of the force is a function of the distance between the two elements, while the frictional damping force depends on the relative velocity of the two elements.

To describe the forces between two elements, we begin by introducing some notation. Let \vec{x}_i , \vec{x}_j be the positions of elements i and j . The distance between elements i and j is

$$d_{ij} = |\vec{x}_i - \vec{x}_j|. \quad (3)$$

When calculating the interactive forces between elements, the elements are assumed to be circular. We define the interaction diameter of an element by

$$D_i = 2 \sqrt{\frac{A_i}{\pi}}, \quad (4)$$

where A_i is the planar surface area of element i . Using this, we define the critical interactive length scale,

$$L_{ij} = \frac{D_i + D_j}{2}, \quad (5)$$

which governs interactions between elements i and j . Repulsive forces are only applied when $d_{i,j} < L_{i,j}$, while for $d_{i,j} > L_{i,j}$ attractive bonded forces are applied when a bond exists between element i and j . Bond and repulsive forces are designed such that in the

absence of other forces, bonded particles will settle in an equilibrium position where elements are separated by the critical interaction length scale $L_{i,j}$.

To aid in notation, we define a bond matrix B_{ij} such that $B_{ij} = 1$ if elements i and j are bonded together and $B_{ij} = 0$ otherwise. Using this notation, the interactive force $(\vec{F}_{IA})_{ij}$ on an element i by an element j is given by

$$(\vec{F}_{IA})_{ij} = \begin{cases} (\vec{F}_e)_{ij} + (\vec{F}_d)_{ij} & \text{if } d_{ij} \leq L_{ij} \\ (\vec{F}_e)_{ij} + (\vec{F}_d)_{ij} & \text{if } d_{ij} > L_{ij} \text{ and } B_{ij} = 1 \\ 0 & \text{if } d_{ij} > L_{ij} \text{ and } B_{ij} = 0 \end{cases} \quad (6)$$

$(\vec{F}_e)_{ij}$ and $(\vec{F}_d)_{ij}$ are the elastic and frictional damping components of the interactive force between elements i and j. The elastic force $(\vec{F}_e)_{ij}$ between elements is given by

$$(\vec{F}_e)_{ij} = -\kappa_e (d_{i,j} - L_{i,j}) T_{i,j} \vec{r}_{ij}, \quad (7)$$

where $\vec{r}_{ij} = \frac{(\vec{x}_i - \vec{x}_j)}{|\vec{x}_i - \vec{x}_j|}$ is the directional unit vector between the position of element i and j, κ_e is the spring constant, and $T_{i,j}$ is the minimum of the thickness of elements i, j. The interactive forces obey Newton's 3rd Law (i.e.: $(\vec{F}_{IA})_{ij} = -(\vec{F}_{IA})_{ji}$). The minimum thickness, $T_{i,j}$, is preferred to the average thickness, since this means that for two bonded elements a fixed distance apart, the acceleration due to elastic forces is bounded, even when the thickness of one of the elements approaches zero.

The frictional damping force has components that damp both the relative radial velocity and relative transverse velocities of the two elements. If \vec{r}_{ij}^\perp is the direction vector perpendicular to \vec{r}_{ij} , and $P_{\vec{r}_{ij}}$ and $P_{\vec{r}_{ij}^\perp}$ are the projection matrices that project onto \vec{r}_{ij} and \vec{r}_{ij}^\perp respectively, then the frictional damping force is given by

$$(\vec{F}_d)_{ij} = \left(-c_r P_{\vec{r}_{ij}} - c_t P_{\vec{r}_{ij}^\perp} \right) \cdot (\vec{u}_i - \vec{u}_j) \quad (8)$$

Here c_r and c_t are the radial and transverse drag coefficients. For the simulation below, we set $c_r = 2\sqrt{\kappa_e}$ and $c_t = \frac{1}{4}c_r$ so that the radial elastic force is critically damped, and the transverse damping is sub critical. The damping forces are implemented using an implicit time stepping scheme, to avoid stability issues for very small elements (details found in Appendix B).

The effectiveness of the repulsive forces can be seen in Figure 8, which shows an uncoupled (ice only) simulation where ice elements drift westward into a bay, and eventually come to rest with minimal overlap between elements. The effectiveness of the numerical bonds is demonstrated in Figure 8, where tabular icebergs (constructed from many ice elements bonded together) and individual icebergs (unbonded elements) drift together towards a convex coast line. When the tabular icebergs arrive at the coast, they bump into the coastline and begin to rotate, influencing the paths of the other icebergs. In this example we see that modeling large structures using small elements bonded together, allows us to achieve large-scale structure and rotational motion, without having to include an equation for the angular momentum of the elements (as discussed in Jakobsen [2001]). Animations of these uncoupled simulations can be found in the supplementary materials.

2.3 Initializing element geometry and packing

For purposes of packing, we assume that elements have surface areas which are shaped as equally-sized regular hexagons (note that the elements are assumed to be circular for purposes of interactions, but are assumed to be hexagonal for packing purposes). When packing these elements together, the hexagonal elements are initially arranged in a staggered lattice, with each element bonded to the adjacent elements (see Figure 8a). In this arrangement, each element (away from the edges) is bonded to six other elements.

187 The bonds between elements form a pattern of equilateral triangles, which give the larger
 188 structure rigidity. The circular shape of elements (used for interactions) is inscribed within
 189 the hexagonal shape used for packing (Figure 8a). The centers of adjacent elements are
 190 initially separated by a distance $d_{i,j} = L_{i,j} = 2A_p$, where A_p is the length the apothems
 191 of the hexagons.

192 Some experiments were also performed using rectangular elements, arranged in a
 193 regular (non-staggered) lattice. In this case, each element forms four bonds with adjacent
 194 elements. However, the resultant structures were found to be much less rigid and tended
 195 to collapse when sufficient forces was applied. For this reason, hexagonal elements are
 196 used here.

197 2.4 Ocean-ice and ice-ocean coupling

198 The LTIM model is coupled to the ocean model via a two-way synchronous cou-
 199pling, meaning that ocean model fields are passed to the LTIM model and the LTIM model
 200 fields are passed back to the ocean model at every time step. Passing fields between the
 201 two models involves interpolating fields between the Eulerian grid of the ocean model and
 202 aggregating the ‘Lagrangian grid’ of the LTIM model (i.e.: onto the ice elements).

203 The coupling from the ocean model to the LTIM model is straight forward: at ev-
 204 ery time step, the ocean mixed layer temperature, salinity, velocity and sea-ice concen-
 205 tration are passed from the ocean model to the LTIM model, to be used in the momen-
 206 tum and thermodynamic equations of the ice elements. Since tabular icebergs are explic-
 207 itly resolved in the ocean, it is sufficient for each element to interact with ocean mixed
 208 layer only (i.e.: there is no need to manually embed icebergs into the ocean by integrating
 209 ocean fields over the icebergs’ thickness, as suggested in Merino et al [2016]). Within the
 210 LTIM model, the ocean model fields are interpolated onto the Lagrangian grid using a bi-
 211 linear interpolation scheme. The LTIM model is not sensitive to the chosen interpolation
 212 scheme.

213 The coupling from the LTIM to ocean model is more complex. The LTIM model
 214 influences the ocean by: (i) applying a pressure to the ocean surface, (ii) imposing heat,
 215 salinity and mass fluxes on the ocean, associated with ice melting, and (iii) affecting the
 216 upper ocean by applying a no-slip boundary condition and frictional velocity beneath the
 217 ice. Fields from the LTIM model are aggregated from the Lagrangian grid to the Eulerian
 218 ocean grid before they are passed to the ocean model. Since LTIM applies large pressures
 219 to the ocean surface, the ocean model is sensitive to the interpolation scheme used to map
 220 the LTIM fields to the ocean grid. Sudden jumps to the ocean surface pressure can trigger
 221 tsunamis within the ocean model, making the ocean model unrealistic.

222 The aggregation of the LTIM fields onto the ocean grid is done in a way that is con-
 223 sistent with the shape of the elements in the LTIM model (see Section 2.3). Fields are
 224 ‘spread’ to the ocean model grid by exactly calculating what fraction of an element’s sur-
 225 face area lies in a particular grid box, and dividing the field in proportion to this fraction.
 226 For example, consider a hexagonal element in the LTIM model, which is positioned such
 227 that it intersects four ocean grid cells (Figure 8b). In this situation, the mass of the ele-
 228 ment is divided between these four ocean cells in proportion to the overlap area between
 229 the hexagonal element and the grid cell (this fraction is shown by the colors in 8b). An
 230 advantage of this approach is that there are no jumps in pressure as an element moves
 231 from one grid cell to another.

232 The numerical calculation of the intersection between hexagons and the ocean grid
 233 is simplified by dividing the hexagon into 6 equilateral triangles. This method allows for
 234 the intersection to be found even when the hexagon is not aligned with the grid.

235 The field-spreading scheme is coded with the restriction that an element's area can
 236 only intersect a maximum of four ocean grid cells at a time. A consequence of this is
 237 that this sets a limit on the maximum size of elements that can be represented using this
 238 model, i.e.: the longest horizontal dimension of an ice element must be smaller than the
 239 ocean grid spacing. Larger ice structures are constructed by bonding together smaller ele-
 240 ments.

241 2.5 Thermodynamics

242 The ice elements decay according to a number of melt parameterizations. As the
 243 ice elements melt, their mass decreases, and the appropriate salt, mass and heat fluxes are
 244 passed to the ocean. In this section we described the melt parametrization for bonded,
 245 unbonded and partially bonded elements.

246 As mentioned above, ice elements which do not interact with other elements are
 247 modeled identically to the point particle icebergs described in Martin and Adcroft [2010].
 248 These elements melt according to three semi-empirical parametrization for melt commonly
 249 used in previous iceberg studies [Gladstone et al , 2001; Martin and Adcroft , 2010].
 250 Three types of iceberg melting are used: basal melt, M_b , melt due to wave erosion, M_e
 251 and melt due to buoyant convection, M_v . M_e and M_v are applied to the sides of the ice
 252 element, while M_b is applied at the ice element base. The details of M_b , M_v and M_e are
 253 given in Appendix A.

254 When multiple elements are bonded together to form larger structures, it is no longer
 255 appropriate to use the parameterizations for melt developed for individual point-particle
 256 icebergs. An element which is completely surrounded by other elements, is meant to rep-
 257 resent a piece of ice in the middle of a large structure, and hence will not experience a
 258 melt at its sides due to wave erosion or buoyant convection. Also, the iceberg basal melt
 259 rate, M_b described above is based on boundary layer theory of flow past a finite plate, and
 260 is only appropriate for basal surfaces where the distance from the leading edge is suffi-
 261 ciently small [Eckert , 1950; Weeks and Campbell , 1973]. For an element in the interior
 262 of large structures, the distance from the edge of the structure is large, and so using M_b
 263 for the basal melt is not appropriate. Instead, the basal melt, M_s is determined using the
 264 three equation model for basal melt, which is a typical melting parametrization beneath
 265 used beneath ice shelves [Holland and Jenkins , 1999].

266 When using both individual elements and bonded elements in the same simulation,
 267 we determine which melt rate parameterizations to use based on the amount of bonds
 268 that each element has. An element which is in the center of a large structure will form
 269 the maximum number of bonds, while unbonded elements form zero bonds. If maximum
 270 number of bonds that an element can form (given the shape of the element) is N_{max} , and
 271 the number bonds that an element has is N_b , then the side melt and bottom melt for that
 272 element are given by

$$M_{side} = \frac{(N_{max} - N_b)}{N_{max}} (M_v + M_e) \quad (9)$$

273 and

$$M_{bottom} = \frac{(N_{max} - N_b)}{N_{max}} M_b + \frac{N_b}{N_{max}} M_s \quad (10)$$

274 respectively. In this way, elements with no bonds, melt like point-particle icebergs, ele-
 275 ments at the center of large structures melt like ice shelves, and elements at the sides of
 276 large structures have a combination of iceberg side and basal melt, and ice-shelf melt.

277 2.6 Algorithms and computational efficiency

278 Including interactions between elements leads to an increase in the computational
 279 complexity of the model. In this subsection we comment on some of the algorithmic pro-
 280 cedures that have been used to increase the computational efficiency.

281 **2.6.1 Interactions and Bonds**

282 At every time step, we calculate the force on each element due to interactions with
 283 every other element. In principle, this involves order N^2 operations (for N elements).
 284 However, since each element only has repulsive interactions with elements that are less
 285 than one ocean grid cell away, and each element only has bonded interactions with a
 286 small number of other elements, we are able to reduce the complexity of the system.

287 The complexity reduction is achieved by storing the element data in an efficient way
 288 that prevents having to search through all element pairs to check if they are close to one
 289 another or are bonded with one another. The data storage system works as follows: point-
 290 ers to the memory structures containing each element are stored in linked list data struc-
 291 tures, which allow elements to be added and removed from the lists easily without re-
 292 structuring the entire list. Instead of using one list for all the elements on a processor (as
 293 was done in the original code [Martin and Adcroft , 2010]), we use a separate linked list
 294 for each ocean grid cell. When an element moves between ocean grid cells, it is removed
 295 from its original list and added to the list corresponding to its new ocean grid cell. Since
 296 the area of elements has to be smaller than the area of an ocean grid cell, the critical in-
 297 teraction length scale (equation 5) is less than the length of a grid cell. This means that
 298 elements only experience repulsive forces with elements in the same ocean grid cell, or
 299 in one of the 8 adjacent cells. Limiting the possible repulsive interactions to elements in
 300 these 9 linked lists substantially reduces the computational time needed to calculate the
 301 total interactive force.

302 Bonded interactions are handled differently. Each bond is assigned a piece of mem-
 303 ory. Each ice element contains a linked list of each of its bonds (typically up to six bonds
 304 per element). At each time step, the code traverses the lists of bonded elements, and adds
 305 a bonded force corresponding to these bond. The bonded force is only applied if $d_{i,j} >$
 306 L_{ij} , to avoid double counting an interaction. Having a list of bonds stored with each ele-
 307 ment reduces the computational complexity of bonded interactions from order N^2 to order
 308 N. Handling bonded attractive forces separately to the repulsive and non-bonded forces
 309 means that we do not need to check whether two elements are bonded, which further in-
 310 creases the computational efficiency.

311 **2.6.2 Parallelization and halos**

312 The LTIM model runs on multiple processors in parallel (and the same grid as the
 313 ocean decomposition). When elements move from an ocean cell on one processor to an
 314 ocean cell on a second processor, the memory has to be passed from one processor the
 315 next, added and removed to the appropriate lists and the memory has to be allocated and
 316 deallocated correctly. Element interactions across the edge of processors are handled us-
 317 ing computational halos. A computational halo is a copy of the edge of a one processor
 318 which is appended to the edge of a second processor, so that the first processor can ‘see’
 319 the second processor during a time step. Before each time step, elements at the edges of
 320 each processor are copied onto the halos of adjacent processors so that they can be used
 321 in calculating the interactive forces. After each time step, these halos are removed, and
 322 the process is repeated. These halo updates are one of the most computationally expensive
 323 parts of the LTIM model.

324 Keeping track of pairs of bonded elements that move across a processor edge re-
 325 quires a lot of book keeping since bonds have to be severed and reconnected. Details of
 326 how the bonds are broken and reconnected across processor boundaries are provided in
 327 Appendix C.

328 **2.6.3 Time stepping**

329 The ice elements in the LTIM model are advected using a semi-implicit velocity
 330 Verlet time-stepping scheme. The velocity Verlet time stepping scheme is commonly used
 331 in DEM models in video games because it is computational efficient and has desirable
 332 stability properties [Jakobsen , 2001]. This time stepping scheme was preferred to the
 333 Runge-Kutta 4, which was used in the iceberg model of Martin and Adcroft [2010] since
 334 the Verlet time stepping only requires a calculation of the interactive forces once per time
 335 step (while the Runge-Kutta scheme requires the interactive forces to be calculated four
 336 times). Since the calculation of the interactive forces is one of the most computationally
 337 expensive part of the algorithm, the Verlet scheme leads to a significant increase in the
 338 speed of the model. We note that the Verlet scheme used in the LTIM contains a modifi-
 339 cation of the original (fully explicit) velocity Verlet time stepping scheme in that damping
 340 terms are treated implicitly (which increases the numerical stability). The details of this
 341 time stepping scheme are outlined in Appendix B.

342 **3 Experiment Setup**

343 The introduction of Lagrangian elements, numerical bonds and interpolation schemes
 344 between the Eulerian and Lagrangian grids (discussed in Section 2) means that we now
 345 have the tools to model giant tabular icebergs submerged in the ocean. We demonstrate
 346 this capability by simulating a tabular iceberg drifting away from an idealized ice shelf.

347 **3.1 Model configuration**

348 We initialized our simulation using the experimental setup created for the Marine
 349 Ice Ocean Modeling Inter-comparison Project (MISOMIP) [Asay-Davis et al , 2016]. The
 350 configuration consists of an idealized ice shelf in a rectangular domain. The domain is
 351 $L_x = 80\text{km}$ wide and $L_y = 480\text{km}$ long, and contains an ice shelf which is grounded on
 352 the south side of the domain and has an ice front at $y=650\text{ km}$. The ice thickness and
 353 bottom topography of this setup are shown in Figure 8a and 8b respectively, with the
 354 grounding line position drawn in for reference. The configuration is the same as that of
 355 the Ocean0 setup in the MISOMIP, with a few minor changes to the ice-shelf geometry
 356 (see Supplementary Material for details).

357 **3.2 Initializing Lagrangian elements:**

358 The idealized ice shelf is constructed out of Lagrangian ice elements. Ice elements
 359 are hexagonal and are arranged in a regular staggered lattice (as discussed in Section 2.3).
 360 The sides of the gridded hexagons are initialized with length $S = 0.98\text{ km}$. Gaps along
 361 the boundaries are filled in using smaller elements so that the total ice-shelf area is pre-
 362 served. The initial mass of the ice elements is determined by a preprocessing inversion
 363 step, which is the inverse of the ‘mass-spreading’ interpolation procedure discussed in
 364 Section 2.3. The pre-interpolation ice draft (treating elements as point masses) contains
 365 large grid artifacts (Figures 8c). These grid artifacts are much reduced after the mass-
 366 spreading interpolation is applied (Figure 8b).

367 **3.3 Ocean model setup**

368 The LTIM model is coupled to the MOM6 ocean model [Hallberg et al , 2013]. The
 369 ocean model is run using a vertical coordinate system which is a hybrid between a sigma-
 370 level and a z-level coordinate. In particular, model layers bend underneath the ice shelf
 371 as they would in a sigma-coordinate model, but collapse to zero thickness when they in-
 372 tersect with bottom topography, as they would in a z-level model. The coordinate system
 373 was achieved using ALE regridding-remapping scheme [White et al , 2009]. The model

uses a horizontal resolution of 2km, and 72 vertical layers. All simulations were repeated using the ocean model configured in isopycnal mode (results were similar and are not presented here).

Ocean parameters are as specified in the MISOMIP configuration [Asay-Davis et al , 2016], and are shown in Table 1. The simulation is initially at rest, with horizontally uniform initial ocean temperature and salinity profiles which vary linearly between specified surface and bottom values: $T_{top} = -1.9^{\circ}\text{C}$, $T_{bottom} = 1.0^{\circ}\text{C}$, $S_{top} = 33.8 \text{ psu}$, $S_{bottom} = 34.7$. The maximum ocean depth is $H_{ocean} = 720 \text{ m}$. A sponge layer is used on the northern boundary, which relaxes back to the initial temperature and salinity with a relaxation time scale of $T_{sponge} = 0.1 \text{ days}$. Melting is set to zero for ocean cells where the ocean column thickness is less than 10m to avoid using more energy to melt ice than is present in the water column.

3.4 Spinup and iceberg calving:

The model is spun up for 5 years with all ice elements being held stationary. After spinup, a giant tabular iceberg is ‘broken off’ from the ice shelf, and allowed to drift into the open ocean. This is achieved by allowing all ice elements initially within a 14.4 km radius of the center of the ice front to move freely while the other ice elements continue to be held stationary. Ice elements less than 12 km from the center of the ice front, are bonded together to form a semi-circular tabular iceberg. A ring of elements whose distance, d , from the ice front center obeys $12 \text{ km} \leq d \leq 14.4 \text{ km}$, are allowed to move freely, but have all their bonds removed. Elements in this half annulus represent fragments of the ice shelf which calve into small pieces during a large calving event. Breaking the bonds of these surrounding elements allows the tabular iceberg to move away from the ice-shelf cavity more easily.

After the spinup period, a wind stress $\vec{\tau} = <\tau_x, \tau_y> = <0.05, 0.05> \frac{N}{m^2}$ is applied to drive the tabular iceberg away from the ice-shelf cavity. Perturbation experiments were performed using other wind stress values.

4 Model Results

During spinup, the injection of buoyant meltwater at the base of the ice shelf drives a clockwise circulation within the domain (not shown). The circulation compares well with an identical static ice-shelf experiment run using an Eulerian ice shelf model [Goldberg et al , 2012] (a detailed comparison of the Lagrangian and Eulerian ice shelf models is presented in a separate study, and is not shown here).

Once spinup is complete, the elements near the ice-shelf front are allowed to move freely, and the icebergs begin to drift away from the ice shelf (see animations in the supplementary materials). The semi-circular tabular iceberg moves as a cohesive unit due to the presence of the numerical bonds, while the smaller ice fragments quickly disperse (Figure 8). The tabular iceberg drifts towards the northward east, driven by the wind and steered by the Coriolis force.

A warming of the surface waters is observed around the tabular iceberg, with the largest warming occurring at the ice-shelf front and along the tabular iceberg’s rounded edge (Figure 8). This surface warming is caused by upwelling of the warmer waters from beneath the ice shelf and iceberg. As the icebergs drifts away from the ice shelf, these warmer waters remain at the surface, mapping of the wake of the iceberg (Figure 8). The signature of upwelling water in the wake of a drifting tabular iceberg bears some similarity to satellite observations of streaks of increased ocean color in the wake of tabular iceberg in the Southern Ocean [Duprat et al , 2016], suggesting that the increased pro-

421 ductivity around icebergs may be driven by upwelling water delivering nutrients to the
 422 surface.

423 The motion of the tabular iceberg disturbs the ocean surface, which drives ocean
 424 velocities through out the water column (Figure 8). The elevated shears around the tabu-
 425 lar iceberg lead to increased vertical mixing in the vicinity of the iceberg, which alters
 426 the stratification of the water column (Figure 8), heating the upper ocean. The increased
 427 ocean velocities and increased surface temperatures cause elevated melt rates at the base
 428 of the ice shelf and iceberg (Figure 8). The largest melt rates are observed at the newly
 429 calved ice-shelf front and on the rounded side of the iceberg (Figure 8a), where the ice-
 430 berg calving has created steep ice cliffs. These sharp ice fronts allow for large ocean
 431 currents (Figure 8c), which drive the elevated melt rates. The elevated melt rates act to
 432 smooth out the ice front over time, making the ice cliff less steep. While this is likely a
 433 real phenomena that could be observed in nature, we should be wary of the modeled ve-
 434 locities at the ice cliffs, since large changes in ice thicknesses are often associated with
 435 numerical pressure gradient errors which can drive spurious motion.

436 As mentioned above, the direction (and speed) of the iceberg drift is largely deter-
 437 mined by the wind speed and direction. Perturbation experiments using different wind
 438 stresses show that for sufficiently large winds, the tabular iceberg drifts to the north east
 439 when $\tau_x > 0$, and to the north west when $\tau_x < 0$ (not shown). For a purely zonal wind
 440 stress with $|\tau_x| \leq 0.01 \frac{N}{m^2}$, the iceberg does not move away from the ice shelf. When the
 441 wind is purely offshore ($\tau_x = 0.0 \frac{N}{m^2}$), a meridional wind stress $\tau_y \geq 0.05 \frac{N}{m^2}$ is needed
 442 to move the tabular iceberg away from the ice shelf. While this result is partly an artifact
 443 of the artificial shape of the calving iceberg, it is also consistent with Bassis and Jacobs
 444 [2013] who noted that calving is a two step process consisting of (i) ice-shelf breaking
 445 and (ii) iceberg detachment. The results here suggest that strong (cross-shore) winds may
 446 be required to drive large tabular icebergs away from their mother glaciers.

447 Finally, we note that the numerical bonds in the LTIM model are needed in order
 448 to allow the tabular iceberg to retain its shape. Comparing the iceberg calving simulation
 449 with an identical simulation where all numerical bonds have been removed, shows that in
 450 the absence of the bonds, the ice elements quickly disperse (Figure 8). In this case, the
 451 model behavior is more similar to an ice-shelf disintegration and does not create a co-
 452 hesive tabular iceberg. By breaking some (but not all) numerical bonds, we can simulate
 453 the fracturing of tabular icebergs, allowing tabular icebergs to break into smaller pieces
 454 (Figure ???). The breaking of a tabular iceberg increases decay rate of the iceberg by in-
 455 creasing the surface area of ice exposed to the ocean. Splitting the tabular iceberg into
 456 smaller fragments also allows the fragments of the iceberg to move more rapidly, and be
 457 more strongly influenced by the wind.

458 5 Summary

459 In this study we present a novel framework for representing tabular icebergs in nu-
 460 matical ocean models. In this framework, giant tabular icebergs are constructed from col-
 461 lections of Lagrangian elements that are held together by numerical bonds. Constructing
 462 tabular icebergs out of many independent elements allows the icebergs to interact with
 463 the ocean across a wide area (larger than a grid cell), and behave as if they had a finite
 464 size and structure. This is in contrast to previous representations of icebergs in numerical
 465 models [Jongma et al , 2009; Martin and Adcroft , 2010; Marsh et al , 2015] that repre-
 466 sent icebergs as point particles. Explicitly resolving tabular icebergs in the ocean allows
 467 the icebergs to interact with the ocean in a more realistic way, and allows us to study the
 468 effect that tabular icebergs have on the ocean circulation. Including numerical bonds be-
 469 tween elements allows for the possibility of breaking bonds to simulation iceberg calving
 470 and fracture.

The capabilities of the tabular iceberg model were demonstrated by modeling a tabular iceberg drifting away from an idealized ice shelf (also constructed using Lagrangian elements). The results show that explicitly resolving the iceberg in the ocean allowed for a complex interaction between the tabular iceberg and the surrounding ocean. In our setup, the tabular iceberg is driven away from the ice shelf by ocean currents, wind stress, and the Coriolis force. As the iceberg moves through the water, it disturbs the ocean surface, driving barotropic ocean currents. The motion of the iceberg and melt beneath the iceberg drive upwelling along the sides of the iceberg, which entrains ambient water and causes a warming of the surface ocean in the wake of the iceberg. The changing ocean conditions feed back onto the iceberg, affecting its motion and melt rates. The highest melt rates are observed at edge of the iceberg which has the steepest ice cliff. These have the effect of smoothing out the ice edge over time. Simulations without using numerical bonds showed that these bonds are essential for allowing the iceberg to move as a unit. We also demonstrate that by breaking these numerical bonds we can simulate iceberg fracture, which is important process that increases the rate of iceberg decay.

To our knowledge, the model presented in this study is the first model to explicitly resolve drifting tabular icebergs in an ocean model that can be used for climate. A natural extension of this work is to try to include tabular icebergs into a general circulation model (GCM) used for climate projections. However, before this can be done, there are a number of issues that need to be resolved: firstly, the question of how and when to introduce tabular icebergs into the ocean needs to be addressed. For GCM's with active ice shelves, a calving law is needed to decide when to release the tabular iceberg into the ocean. The question of what calving law to use is a topic of ongoing research [Benn et all , 2007; Alley et al , 2008; Levermann et al , 2012; Bassis and Jacobs , 2013] and is still unresolved. One potential way to temporarily bypass this problem would be to run hindcast simulations using historically observed calving events. A related issue is the question of how and when to break the bonds within the freely floating icebergs to simulation iceberg breakup. Without a rule for iceberg breakup, the tabular icebergs would likely drift to unrealistically low latitudes. Finally, further work is needed to understand (and model) the interactions between tabular icebergs and sea ice, and to parametrize the effects of iceberg grounding, as these interactions play a large role in dictating the trajectories of tabular icebergs. None-the-less, the technical framework described in this article is potentially a using step towards including tabular icebergs in global GCM's, and hence a step towards making more accurate projections of future sea level.

6 Appendix A

6.1 Environmental forces on ice elements

The non-interactive forces on an ice element are as described in [Martin and Adcroft , 2010], and are repeated here for completeness. The forces on an element due to air (a), ocean (o) and sea ice (si) drag are given by

$$(\vec{F}_a) = \rho_a (0.5c_{a,v}WF + c_{a,h}LW)|\vec{u}_a - \vec{u}|(\vec{u}_a - \vec{u}), \quad (11)$$

$$(\vec{F}_o) = \rho_o (0.5c_{o,v}W(D - T_{si})F + c_{o,h}LW)|\vec{u}_o - \vec{u}|(\vec{u}_o - \vec{u}), \quad (12)$$

$$(\vec{F}_{si}) = \rho_{si} (0.5c_{si,v}WT_{si}F + c_{si,h}LW)|\vec{u}_{si} - \vec{u}|(\vec{u}_{si} - \vec{u}). \quad (13)$$

Here ρ_a , ρ_o , ρ_{si} , are the density of air, ocean and sea ice, respectively. $c_{a,v}$, $c_{o,v}$ and $c_{si,v}$ are the vertical drag coefficients with air, ocean and sea ice, while $c_{a,h}$, $c_{o,h}$ and $c_{si,h}$ are the respective horizontal drag coefficients. \vec{u}_a , \vec{u}_o , \vec{u}_{si} , are the velocities air, ocean and sea ice, respectively. L, W, T, F and D are the length, width, thickness, free-board and draft of the ice element. The element thickness is related to the draft and free-board by $T = F + D$ and $D = \frac{\rho}{\rho_o}T$, where ρ is the ice element density. T_{si} is the sea ice thickness.

519 The wave radiation force (\vec{F}_R) is given by

$$\vec{F}_R = \frac{1}{2} \rho_o c_r g a \min(a, F) 2 \frac{WL}{W+L} \frac{\vec{v}_a}{|\vec{v}_a|} \quad (14)$$

520 where g is the acceleration due to gravity, a is the wave amplitude empirically related to
521 the wind speed by $a = 0.010125|\vec{v}_a - \vec{v}_o|$, and c_{wd} is the wave drag coefficient defined as

$$c_{wd} = 0.06 \min\left(\max\left[0, \frac{L - L_c}{L_t - L_c}\right], 1\right), \quad (15)$$

522 where $L_w = 0.32|\vec{v}_a - \vec{v}_o|^2$ is an empirical wave length, $L_c = 0.125L_w$ is the cutoff length,
523 and $L_t = 0.25L_w$ is the upper limit.

524 The pressure gradient force is approximated as a force due to sea surface slope and
525 given by

$$\vec{F}_{SS} = -Mg\vec{\nabla}\eta \quad (16)$$

526 where η is the sea surface height.

527 6.2 Melt rate parametrization

528 As discussed in Section 2.5, unbounded ice elements in the LTIM model decay ac-
529 cording to parameterizations for iceberg decay typically used in iceberg drift models [Mar-
530 tin and Adcroft , 2010], while ice elements within larger ice structures have only a basal
531 melt given by the three equation model [Holland and Jenkins , 1999] .

532 For unbonded ice elements, the element thickness decays due to basal melt at a rate
533 M_b , while the length and width of the elements decay as a result of melt due to wave ero-
534 sion, M_e , and melt due to buoyant convection, M_v . Following Gladstone et al [2001] and
535 Martin and Adcroft [2010], the basal melt rate, wave erosion melt rate, and buoyant con-
536 vection melt rate are parameterized by

$$M_b = 0.58|\vec{v} - \vec{v}_0|^{0.8} \frac{\tilde{T}_0 - \tilde{T}}{L^{0.2}} \quad (17)$$

$$M_e = \frac{1}{12} S_s \left(1 + \cos[\pi A_i^3]\right) \left(\tilde{T}_0 + 2\right), \quad (18)$$

$$M_v = \left(7.62 \times 10^{-3}\right) \tilde{T}_0 + \left(1.29 \times 10^{-3}\right) \tilde{T}_0^2. \quad (19)$$

539 \tilde{T} is the effective iceberg temperature and is set to $\tilde{T} = 4^\circ\text{C}$, \tilde{T}_0 is the temperature at the
540 top of the ocean, A_i is the sea ice area fraction, and S_s is the sea state, which is given by
541 the Beaufort scale

$$S_s = \frac{2}{3} |\vec{u}_a - \vec{u}_o|^{\frac{1}{2}} + \frac{1}{10} |\vec{u}_a - \vec{u}_o| \quad (20)$$

542 All three melt rates are in units of meters per day.

543 For elements inside larger structures, the melt due to wave erosion and melt due to
544 buoyant convection are set to zero, and the basal melt, M_s is given by the standard three
545 equation model [Holland and Jenkins , 1999].

546 7 Appendix B

547 7.1 Modified Verlet Algorithm

548 The LTIM model uses a version velocity Verlet time-stepping algorithm, which has
549 been modified to allow part of the forcing to be calculated implicitly. The traditional ve-
550 locity Verlet algorithm is commonly used in molecular dynamics, as it is simple to imple-
551 ment, second order accurate and computationally efficient [Swope et al , 1982; Omelyan

et al., 2002]. Here we modify the traditional scheme to allow for the drag forces to be modeled implicitly, which prevents large accelerations for element's whose mass approaches zero. To do this, we include both an implicit and explicit acceleration, $a = a^{exp} + a^{imp}$. The explicit acceleration, a^{exp} includes all forcing terms which depend only on the previous time step and the current position, while the implicit acceleration, a^{imp} includes forcing terms which depend on the velocity at the current time step (in particular the drag and Coriolis forces).

Using a time step of Δt , and subscripts to denote the time step (so that $t_{n+1} = t_n + \Delta t$), the modified velocity Verlet scheme can be written as:

$$1) x_{n+1} = x_n + u_n \Delta t + \frac{1}{2} \Delta t^2 \left(a_n^{exp} + a_n^{imp} \right).$$

$$2) \text{Calculate } a_{n+1}^{exp}$$

$$3) \text{Calculate } a_{n+1}^{imp} \text{ and } u_{n+1} = u_n + \frac{\Delta t}{2} \left(a_n^{exp} + a_{n+1}^{exp} \right) + (\Delta t) a_{n+1}^{imp}$$

This scheme reduces to the traditional velocity Verlet when a^{imp} is set to zero.

Note that $a_{n+1}^{exp} = a_{n+1}^{exp}(x_{n+1}, t_n)$ is an explicit function of x_{n+1} and other quantities evaluated at time t_n , while $a_{n+1}^{imp} = a_{n+1}^{imp}(u_{n+1}, x_{n+1}, t_n)$ additionally depends on u_{n+1} , and needs to be solved implicitly. For this reason in step three, a_{n+1}^{imp} and u_{n+1} need to be solved simultaneously, as described in the next subsection.

In equation (1), the forces due to ocean drag, atmospheric drag and sea ice drag are treated implicitly. The force due to sea surface slope and wave radiation are treated explicitly. The Coriolis term is handled using Crank-Nicolson scheme so that half of the effect is implicit and half is explicit. The elastic part of the interactive forces is treated explicitly, while the interactive damping is handled semi-implicitly in that the drag force on element A by element B depends on the velocities of elements A and B evaluated at time t_{n+1} and t_n , respectively.

7.2 Solving for the velocity implicitly

Since this modified scheme contains some forcing terms which are handled implicitly, a_{n+1}^{imp} and u_{n+1} need to be calculated simultaneously. We demonstrate how this is done, using a simplified one-dimensional version of equation (1), neglecting the atmospheric drag, sea ice drag and Coriolis force, so that the only implicitly treated term is the ocean drag. In this demonstration, we use a superscript to denote the ocean drag force, F^o , and ocean velocity, u^o , to avoid confusion with the subscripts indicating time step. We also define an explicit force, F^{exp} , which accounts for all forces not proportional the element velocity. With these simplifications, the implicit and explicit accelerations are

$$a^{exp} = \frac{1}{M} (\vec{F}^{exp}) \quad (21)$$

$$a^{imp} = \frac{1}{M} (F^o) \quad (22)$$

The ocean drag force at time t_{n+1} is modeled (mostly) implicitly as

$$F_{n+1}^o = \tilde{c}^o |u_n^o - u_n| (u_n^o - u_{n+1}), \quad (23)$$

where \tilde{c}^o is the effective drag coefficient, accounting for the dimensions of the ice element (see equation 12).

Step 3 of the modified velocity Verlet scheme can be rewritten by introducing an intermediate velocity u^* , which only depends on the velocity and acceleration at time t_n ,

$$u_n^* = u_n + \frac{1}{2} (\Delta t) a_n^{exp}. \quad (24)$$

Using this, the updated velocity (Step 3) can be written

$$u_{n+1} = u_n^* + \frac{\Delta t}{2} a_{n+1}^{exp} + (\Delta t) a_{n+1}^{imp}. \quad (25)$$

592 Including the forcing terms into this equations gives

$$u_{n+1} = u_n^* + \frac{\Delta t}{2M} (F_{n+1}^{exp}) + \frac{\Delta t}{M} \left(c_w |u_n^o - u_n| (u_n^o - u_{n+1}) \right) \quad (26)$$

593 Solving for $u(t_{n+1})$ in terms of quantities which only depend on the previous time step
594 gives

$$u_{n+1} = \frac{u_n^* + \frac{\Delta t}{2M} (F_{n+1}^{exp}) + \frac{\Delta t}{M} \left(c_w |u_n^o - u_n| (u_n^o) \right)}{\left(1 + \frac{\Delta t}{M} c_w |u_n^o - u_n| \right)} \quad (27)$$

595 Once the u_{n+1} has been found, it can be used to calculate the explicit and implicit acceler-
596 ations, which are required for the next time step.

597 Finally, we note that the the drag term (equation 23) is not entirely implicit, since
598 the element velocity inside the absolute value is evaluated at time t_n , rather than at time
599 t_{n+1} . This is done so that we can solve for the updated velocity analytically. One conse-
600 quence of this is that it can give rise to a small oscillation in the element velocity. This
601 oscillation is addressed by using a predictive corrective scheme: after solving for a first
602 guess of the velocity at time t_{n+1} , this estimate of the velocity is used to update the esti-
603 mate of the drag force (i.e.: inside the absolute value signs). This updated drag, can now
604 be used to repeat the process described above to find an improved estimate of the velocity.
605 We found that two iterations were sufficient to remove the unwanted oscillation.

606 The procedure described in this section is easily extended to include more forcing
607 terms and two dimensions (where it involves inverting a 2×2 matrix).

608 8 Appendix C

609 Connecting bonds across processor boundaries

610 Since the LTIM model is parallelized across multiple processors, it often happens
611 that two elements on different processes are bonded together. Keeping track of numeri-
612 cal bonds across processor boundaries requires a lot of book keeping. In this section we
613 describe the how LTIM model handles bonds across processor boundaries.

614 The basics of the bond bookkeeping work as follows: consider an element A and
615 an element B that are bonded together. Each element has a copy of the bond (a piece of
616 memory which describes the bond between the two elements), which is stored with the
617 element. Let A-B be the bond stored by element A, and B-A be the bond stored by ele-
618 ment B. Bond A-B contains a pointer which points to element B and bond B-A contains a
619 pointer which points to element A.

620 Consider a situation where element A and B are originally on Processor 1, and then
621 element B moves to Processor 2. When this occurs, the memory assigned to element B
622 on processor 1 is removed, and is allocated on Processor 2. This means that the pointer
623 to element B in bond A-B (stored in element A on Processor 1) is no longer assigned.
624 Similarly, the pointer to element A in bond B-A (stored in element B on Processor 2) is
625 no longer assigned. Before the next time step, a halo update occurs, so that the there is
626 a copy of element A in the halo of Processor 2 and a copy of element B in the halo of
627 Processor 1. After the halo update, the bonds A-B and B-A have to be reconnected on
628 both Processor 1 and 2. To aid in reconnecting the bonds, a copy of the grid cell number
629 of element B is stored in the bond A-B and a copy of the grid cell number of element A
630 is stored in the bond B-A. We refer to this as the ‘most recent address’. Before a bond
631 is moved from one processor to another, the ‘most recent address’ is updated, so that the
632 bond can be reconnected later. To reconnect bond A-B on Processor 1 (for example), we
633 find the most recent address of element B, and search through the list of elements in the

634 grid cell corresponding to the most recent address of element B until element B is found.
635 The pointer to element B in bond A-B is reassigned and the bond is said to be connected.

636 Once all bonds are reconnected, a bond quality control is done where we loop through
637 all bonds and check that they are working properly. To check that a bond is working prop-
638 erly is a four step process. For example, consider the bond A-B stored in element A on
639 Processor 1. To check the quality of this bond, we use the following four steps:

- 640 1. Check that the pointer to element B is assigned on bond A-B (stored on element
641 A).
642 2. Check that the corresponding bond B-A exists on element B.
643 3. Check that a pointer to element A exists in this bond B-A.
644 4. Check that the element A which is being pointed to is the same element A where
645 you started.

646 All four of these tests must pass in order to make sure that the memory is correctly as-
647 signed. A useful tool in this process is that each element is assigned a unique number so
648 that elements are easily identified.

649

Acknowledgments

650

= enter acknowledgments here =

651 References

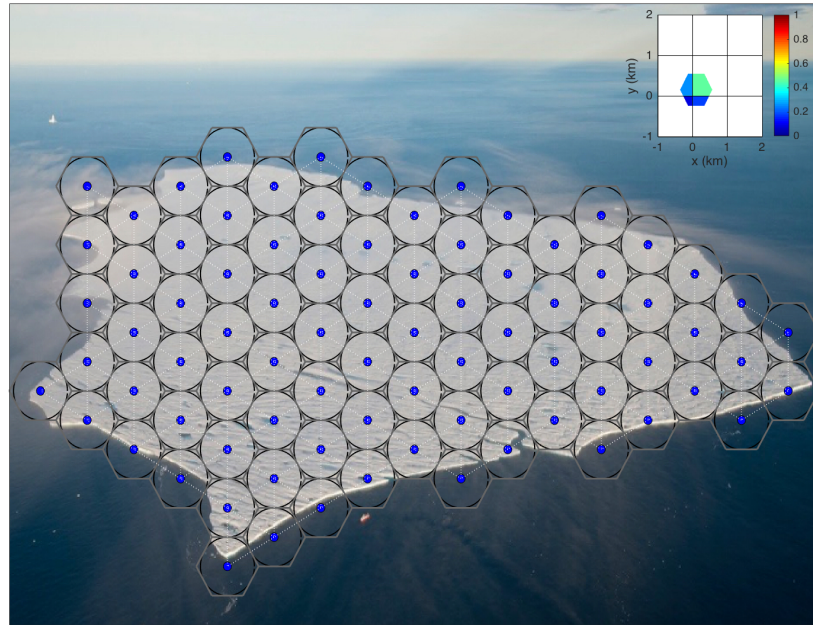
- 652 Asay-Davis, X. S., S. L. Cornford, B. K. Galton-Fenzi, R. M. Gladstone, G. H. Gud-
 653 mundsson, D. M. Holland, P. R. Holland, and D. F. Martin (2016), Experimental de-
 654 sign for three interrelated marine ice sheet and ocean model intercomparison projects:
 655 MISMIP v. 3 (MISMIP+), ISOMIP v. 2 (ISOMIP+) and MISOMIP v. 1 (MISOMIP1).
 656 *Geoscientific Model Development* 9, no. 7: 2471.
- 657 Arrigo, K. R., G. L. van Dijken, D. G. Ainley, M. A. Fahnestock, and T. Markus (2002).
 658 Ecological impact of a large Antarctic iceberg. *Geophys. Res. Lett.*, 29(7).
- 659 Alley, R. B., H. J. Horgan, I. Joughin, K. M. Cuffey, T. K. Dupont, B. R. Parizek, S.
 660 Anandakrishnan, and J. Bassis (2008), A simple law for ice-shelf calving. *Science* 322,
 661 no. 5906, 1344-1344.
- 662 Bassis, J. N., and S. Jacobs (2013), Diverse calving patterns linked to glacier geometry.
 663 *Nature Geoscience*, 6(10), 833-836.
- 664 Benn, D. I., C. R. Warren, and R. H. Mottram (2007). Calving processes and the dynam-
 665 ics of calving glaciers. *Earth-Science Reviews*, 82(3), 143-179.
- 666 Bigg, G. R., Wadley, M. R., Stevens, D. P., and Johnson, J. A. (1997), Modeling the dy-
 667 namics and thermodynamics of icebergs. *Cold Regions Science and Technology*, 26(2),
 668 113-135.
- 669 Borstad, C. P., A. Khazendar, E. Larour, M. Morlighem, E. Rignot, M. P. Schodlok, and
 670 H. Seroussi (2012), A damage mechanics assessment of the Larsen B ice shelf prior to
 671 collapse: Toward a physically-based calving law, *Geophys. Res. Lett.*, 39, L18502
- 672 Biddle, L. C., J. Kaiser, K. J. Heywood, A. F. Thompson and A. Jenkins (2015), Ocean
 673 glider observations of iceberg-enhanced biological productivity in the northwestern
 674 Weddell Sea, *Geophys. Res. Lett.*, 42, 459-465.
- 675 De Rydt, J., and G. H. Gudmundsson (2016), Coupled ice shelf ocean modeling and com-
 676 plex grounding line retreat from a seabed ridge. *J. of Geophys. Res.: Earth Surface*,
 677 121(5), 865-880.
- 678 Dunne, J.P., J.G. John,, A.J. Adcroft, S.M. Griffies, R.W. Hallberg, E. Shevliakova, R.J.
 679 Stouffer, W. Cooke, K.A. Dunne, M.J Harrison, and J.P. Krasting (2012), GFDL's
 680 ESM2 global coupled climate-carbon Earth System Models. Part I: Physical formula-
 681 tion and baseline simulation characteristics. *J. of Climate*, 25(19), 6646-6665.
- 682 Depoorter, M. A., J. L. Bamber, J. A. Griggs, J. T. M. Lenaerts, Stefan RM Ligtenberg,
 683 M. R. van den Broek, and G. Moholdt (2013), Calving fluxes and basal melt rates of
 684 Antarctic ice shelves. *Nature*, 502(7469), 89-92.
- 685 Determan J., Gerdes R. (1994), Melting and freezing beneath ice shelves: implications
 686 from a three-dimensional ocean-circulation model. *Ann. Glaciol.*, 20, 413-419.
- 687 Dowdeswell, J. A., and J. L. Bamber (2007), Keel depths of modern Antarctic icebergs
 688 and implications for sea-floor scouring in the geological record. *Marine Geology*,
 689 243(1), 120-131.
- 690 Duprat, L. P., G. R. Bigg, and D. J. Wilton (2016), Enhanced Southern Ocean marine pro-
 691 ductivity due to fertilization by giant icebergs. *Nature Geoscience*.
- 692 Eckert, E. R. G. (1950). Introduction to the Transfer of Heat and Mass. McGraw-Hill.
- 693 Gladstone, R. M., G. R. Bigg, and K. W. Nicholls. (2001), Iceberg trajectory mod-
 694 eling and meltwater injection in the Southern Ocean (1978-2012). *J. of Geophys. Res.:
 695 Oceans*, 106(C9), 19903-19915.
- 696 Goldberg, D. N., C. M. Little, O. V. Sergienko, A. Gnanadesikan, R. Hallberg, and M.
 697 Oppenheimer (2012), Investigation of land ice-ocean interaction with a fully coupled
 698 ice-ocean model: 1. Model description and behavior. *J. of Geophys. Res.: Earth Surface*,
 699 117(F2).
- 700 Gladish, C. V., D. M. Holland, P. R. Holland, and S. F. Price (2012), Ice-shelf basal chan-
 701 nels in a coupled ice/ocean model. *J. of Glaciol.*, 58(212), 1227-1244.
- 702 Grosfeld K., R. Gerdes, J. Determan (1997), Thermohaline circulation and interaction
 703 between ice shelf cavities and the adjacent open ocean. *J. Phys. Oceanogr.*, 102, C7,

- 704 15959-15610.
- 705 Grosfeld, K., and H. SandhLger, (2004). The evolution of a coupled ice shelfDocean sys-
706 tem under different climate states. *Global and Planetary Change*, 42(1), 107-132.
- 707 Hallberg, R., A. Adcroft, J. P. Dunne, J. P., Krasting, R. J., and Stouffer (2013), Sensitiv-
708 ity of twenty-first-century global-mean steric sea level rise to ocean model formulation.
709 *J. of Climate*, 26(9), 2947-2956.
- 710 Holland D. M., Jenkins A. (2001), Adaptation of an isopycnic coordinate ocean model for
711 the study of circulation beneath ice shelves. *Mon. Wea. Rev.*, 129, 1905-1927.
- 712 Holland P. R. and D. L. Feltham (2006), The effects of rotation and ice shelf topography
713 on frazil-laden Ice Shelf Water plumes. *J. Phys. Oceanogr.*, 36, 2312-2327.
- 714 Holland, D. M., and A. Jenkins (1999), Modeling thermodynamic ice-ocean interactions at
715 the base of an ice shelf. *J. of Phys. Oceanogr.* 29.8, 1787-1800.
- 716 Hellmer H.H., Olbers D. J. (1989), A two-dimensional model for the thermohaline circula-
717 tion under an ice shelf. *Antarctic Science*, 1, 325- 336.
- 718 Henderson J., J. S. P. Loe (2016), The Prospects andChallenges for Arctic Oil Develop-
719 ment. *Oil, Gas and Energy Law Journal (OGEL)*, 14 (2)
- 720 Hopkins, M. A. (1996). On the mesoscale interaction of lead ice and floes. *J. of Geophys.*
721 *Res.: Oceans*, 101(C8), 18315-18326.
- 722 Gaskill, H. S., and J. Rochester (1984). A new technique for iceberg drift prediction. *Cold*
723 *Reg. Sci. Technol.*, 8(3), 223-234.
- 724 Jakobsen, T. (2001). Advanced character physics. In *Game Developers Conference*, Vol. 3.
- 725 Jenkins, A., P. Dutrieux, S. S. Jacobs, S. D. McPhail, J. R. Perrett, A. T. Webb, and D.
726 White (2010), Observations beneath Pine Island Glacier in West Antarctica and implica-
727 tions for its retreat. *it Nature Geo.*, 3(7), 468-472.
- 728 Jacobs, S. S., A. Jenkins, C. F. Giulivi, and P. Dutrieux (2011). Stronger ocean circulation
729 and increased melting under Pine Island Glacier ice shelf. *Nature Geo.*, 4(8), 519-523.
- 730 Jongma, J. I., E. Driesschaert, T. Fichefet, H. Goosse, and H. Renssen (2009), The ef-
731 fect of dynamic-thermodynamic icebergs on the Southern Ocean climate in a three-
732 dimensional model, *Ocean Modell.*, 26, 104Ð113.
- 733 Kubat I., M. Sayed, S. Savage, T. Carrieres (2005), An operational model of iceberg drift
734 *Int. J. Off. Polar Eng.*, 15 (2), 125Ð131
- 735 Lewis E.L. and R.G. Perkin (1986), Ice pumps and their rates. *J. of Geophys. Res.*, 91,
736 11756-11762.
- 737 Losch, M. (2008). Modeling ice shelf cavities in a z coordinate ocean general circulation
738 model. *J. of Geophys. Res.: Oceans*, 113(C8).
- 739 Li, B., H. Li, Y. Liu, A. Wang and S. Ji (2014), A modified discrete element model for
740 sea ice dynamics. *Acta Oceanologica Sinica*, 33(1), 56-63.
- 741 Liu, M. B. and G. R. Liu (2010), Smoothed particle hydrodynamics (SPH): an overview
742 and recent developments. *Archives of computational methods in engineering*, 17(1), 25-
743 76.
- 744 Lichey, C., and H. H. Hellmer (2001). Modeling giant-iceberg drift under the influence of
745 sea ice in the Weddell Sea, Antarctica. *J. of Glaciol.*, 47(158), 452-460.
- 746 Levermann, A., T. Albrecht, R. Winkelmann, M. A. Martin, M. Haseloff, and I. Jougin.
747 (2012), Kinematic first-order calving law implies potential for abrupt ice-shelf retreat.
748 *The Cryosphere*, 6(2), 273-286.
- 749 Mountain, D. G. (1980). On predicting iceberg drift. *Cold Reg. Sci. Technol.*, 1(3-4), 273-
750 282.
- 751 Martin, T., and Adcroft, A. (2010), Parameterizing the fresh-water flux from land ice to
752 ocean with interactive icebergs in a coupled climate model. *Ocean Modelling*, 34(3),
753 111-124.
- 754 Marsh, R., V. O. Ivchenko, N. Skliris, S. Alderson, G. R. Bigg, G. Madec, A. T. Blaker
755 Y. Aksenov, B. Sinha, A.C. Coward, and J.L. Sommer (2015), NEMODICB (v1. 0):
756 interactive icebergs in the NEMO ocean model globally configured at eddy-permitting

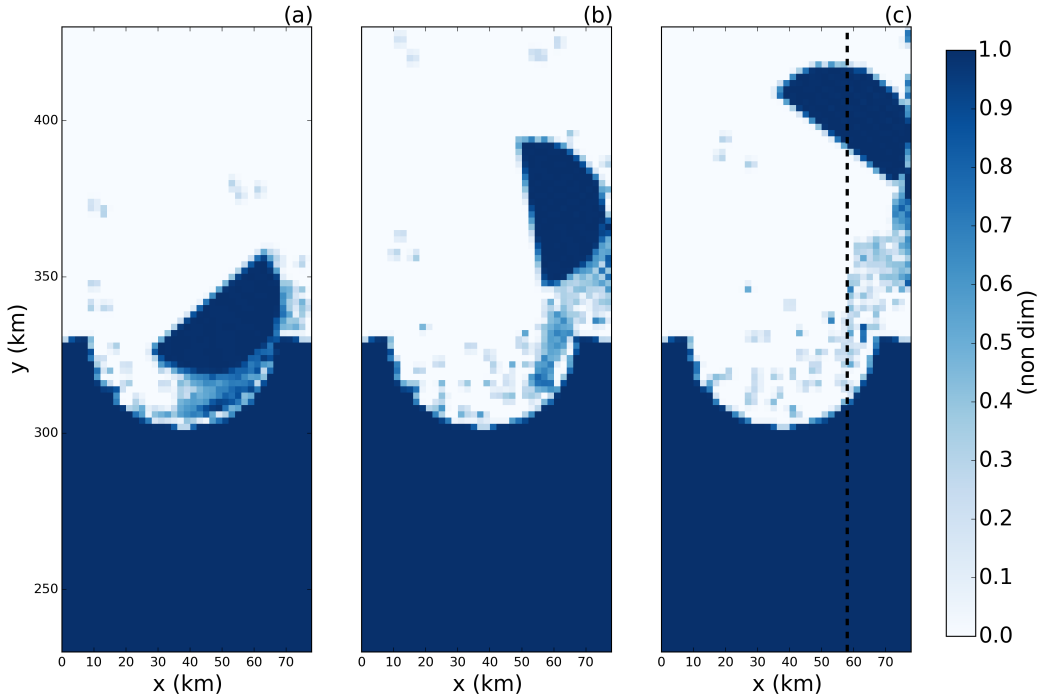
- resolution. *Geoscientific Model Development* 8, no. 5 (2015): 1547-1562.
- MacAyeal D.R. (1984), Thermohaline Circulation Below the Ross Ice Shelf: A Consequence of Tidally Induced Vertical Mixing and Basal Melting. *J. Geophys. Res.*, 89, 597-606
- Merino, N., Le Sommer, J., Durand, G., Jourdain, N. C., Madec, G., Mathiot, P., and Tournadre, J. (2016), Antarctic icebergs melt over the Southern Ocean: climatology and impact on sea ice. *Ocean Modelling*, 104, 99-110.
- Nicholls K.W. (1996), Temperature variability beneath Ronne Ice Shelf, Antarctica, from thermistor cables. *J. Phys. Oceanogr.*, 11, 1199-1210.
- Nicholls KW, Østerhus S, Makinson K (2009), Ice-Ocean processes over the continental shelf of the southern Weddell Sea, Antarctica: a review. *Rev. Geophys.* 47(3).
- Omelyan, I. P., M. I. Mryglod, and R. Folk (2002), Optimized Verlet-like algorithms for molecular dynamics simulations. *Physical Review E*, 65(5), 056706.
- Rignot, E., S. Jacobs, J. Mouginot, and B. Scheuchl (2013), Ice-shelf melting around Antarctica. *Science*, 341, no. 6143 (2013): 266-270.
- Robinson, N. J., M. J. M. Williams, P. J. Barrett, and A. R. Pyne (2010), Observations of flow and ice-ocean interaction beneath the McMurdo Ice Shelf, Antarctica, *J. Geophys. Res.*, 115, C03025
- Pizzolato, L., S. E. Howell, C. Derksen, J. Dawson, L. Copland (2014), Changing sea ice conditions and marine transportation activity in Canadian Arctic waters between 1990 and 2012, *Climatic Change* 123 (2), 161173.
- Pan, W., A. M. Tartakovsky, and J. J. Monaghan (2013), Smoothed particle hydrodynamics non-Newtonian model for ice-sheet and ice-shelf dynamics. *J. of Comp. Phys.*, 242, 828-842.
- Pralong, A., and M. Funk (2005), Dynamic damage model of crevasse opening and application to glacier calving, *J. Geophys. Res.*, 110, B01309.
- Sergienko, O. V. (2013). Basal channels on ice shelves. *J. of Geophys. Res.: Earth Surface*, 118(3), 1342-1355.
- Silva, T. A. M., Bigg, G. R., and Nicholls, K. W. (2006), Contribution of giant icebergs to the Southern Ocean freshwater flux. *J. of Geophys. Res.: Oceans*, 111(C3).
- Smith, K., B. Robison, J. Helly, R. Kaufmann, H. Ruhl, H., T. Shaw, and M. Vernet (2007), Free-drifting icebergs: Hotspots of chemical and biological enrichment in the Weddell Sea, *Science*, 317, 478-482.
- Shepherd, A., and D. Wingham (2007). Recent sea-level contributions of the Antarctic and Greenland ice sheets. *Science*, 315(5818), 1529-1532.
- Stern, A. A., D. M. Holland, P. R. Holland, A. Jenkins and J. Sommeria (2014), The effect of geometry on ice shelf ocean cavity ventilation: a laboratory experiment. *Experiments in Fluids*, 55(5), 1-19.
- Stern, A.A., Johnson, E., Holland, D.M., Wagner, T.J., Wadhams, P., Bates, R., Abrahamson, E.P., Nicholls, K.W., Crawford, A., Gagnon, J. and Tremblay, J.E. (2015), Wind-driven upwelling around grounded tabular icebergs. *J. of Geophys. Res.: Oceans*, 120(8), 5820-5835.
- Stern, A. A., A. Adcroft, and O. Sergienko (2016), The effects of Antarctic iceberg calving size distribution in a global climate model. *J. of Geophys. Res.: Oceans*, 121(8), 5773-5788.
- Swope, W. C., H. C. Andersen, P. H. Berens, and K. R. Wilson (1982), A computer simulation method for the calculation of equilibrium constants for the formation of physical clusters of molecules: Application to small water clusters. *The Journal of Chemical Physics* 76, no. 1, 637-649.
- Tournadre, J., N. Bouhier, F. Girard-Ardhuin, and F. RÖmy (2016), Antarctic icebergs distributions 1992-2014. *J. Geophys Res: Oceans*.
- Turnbull I.D., N. Fournier, M. Stolwijk, T. Fosnaes, D. McGonigal (2015), Operational iceberg drift forecasting in Northwest Greenland, *Cold Reg. Sci. Technol.* 110, 1-18

- 810 Unger, J. D., 2014. Regulating the Arctic Gold Rush: Recommended Regulatory Reforms
 811 to Protect Alaska's Arctic Environment from Offshore Oil Drilling Pollution . *Alaska L.*
 812 *Rev*, 31
- 813 Vernet, M., et al. (2012), Islands of ice: Influence of free-drifting Antarctic icebergs on
 814 pelagic marine ecosystems, *Oceanography*, 25(3), 38Ð39
- 815 Wagner, T. J., Wadhams, P., Bates, R., Elosegui, P., Stern, A., Vella, D., E. P. Abraham-
 816 sen, A. Crawford, and Nicholls, K. W. (2014), The ÐfootlooseÓ mechanism: Iceberg
 817 decay from hydrostatic stresses. *Geophys. Res. Lett.*, 41(15), 5522-5529.
- 818 Weeks, W. F., and W. J. Campbell (1973). Icebergs as a fresh-water source: an appraisal.
 819 *J. of Glaciol.*, 12(65), 207-233.
- 820 White, L., A. Adcroft, and R. Hallberg (2009), High-order regridding-remapping schemes
 821 for continuous isopycnal and generalized coordinates in ocean models. *J. of Comp.*
 822 *Phys.*, 228(23), 8665-8692.

Parameter	Symbol	Value	Unit
Domain Length	L_x	80	km
Domain Width	L_y	480	km
Horizontal Resolution	Δx	2	km
Number of vertical layers	N_l	72	non-dim
Horizontal Viscosity	ν_H	6.0	$\frac{m^2}{s}$
Diapycnal Viscosity	ν_V	10^{-3}	$\frac{m^2}{s}$
Horizontal Diffusivity	ϵ_H	1.0	$\frac{m^2}{s}$
Diapycnal Diffusivity	ϵ_V	5×10^{-5}	$\frac{m^2}{s}$
Initial Surface Temperature	T_t	-1.9	$^{\circ}C$
Initial Bottom Temperature	T_b	1.0	$^{\circ}C$
Initial Surface Salinity	S_t	33.8	psu
Initial Bottom Salinity	S_b	34.7	psu
Maximum Ocean depth	H_{ocean}	720	m
Relaxation Time of Sponge Layer	T_{sponge}	0.1	days
Time Step for Static Shelf Experiment	dt_{Static}	1000	s
Time Step for Iceberg Calving Experiment	$dt_{Calving}$	10	s

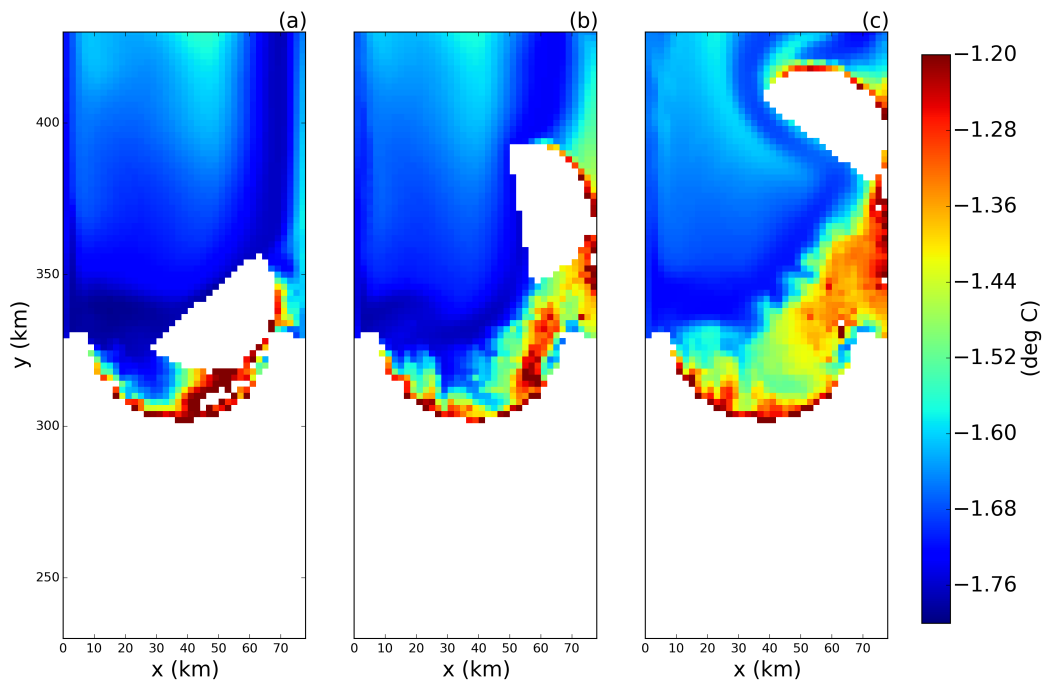


823 **Figure 1.** Schematic showing how Lagrangian elements are used when modeling tabular icebergs. La-
 824 grangian elements (blue dots) are initialized in a staggered lattice covering the surface area of the iceberg.
 825 For purposes of mass aggregation, the ice elements are assumed to have hexagonal shape (grey hexagons).
 826 For purposes of element interactions, the ice elements are assumed to be circular (black circles). Elements
 827 are initially bonded to adjacent elements using numerical bonds (dashed white lines). These numerical bonds
 828 form equilateral triangles which give the shape rigidity. The inset panel shows a schematic of the intersection
 829 of a hexagonal element and the ocean grid. The colors indicate the fraction of the hexagon that lies in each
 830 grid cell. These fractions are used as weights to spread LTIM properties to the ocean grid (see text for more
 831 details) The background photo in the larger schematic is an areal photograph of iceberg PIIB (Area= 42 km²)
 832 taken in Baffin Bay in 2012. The red ship can be identified on the bottom of the photo for scale.

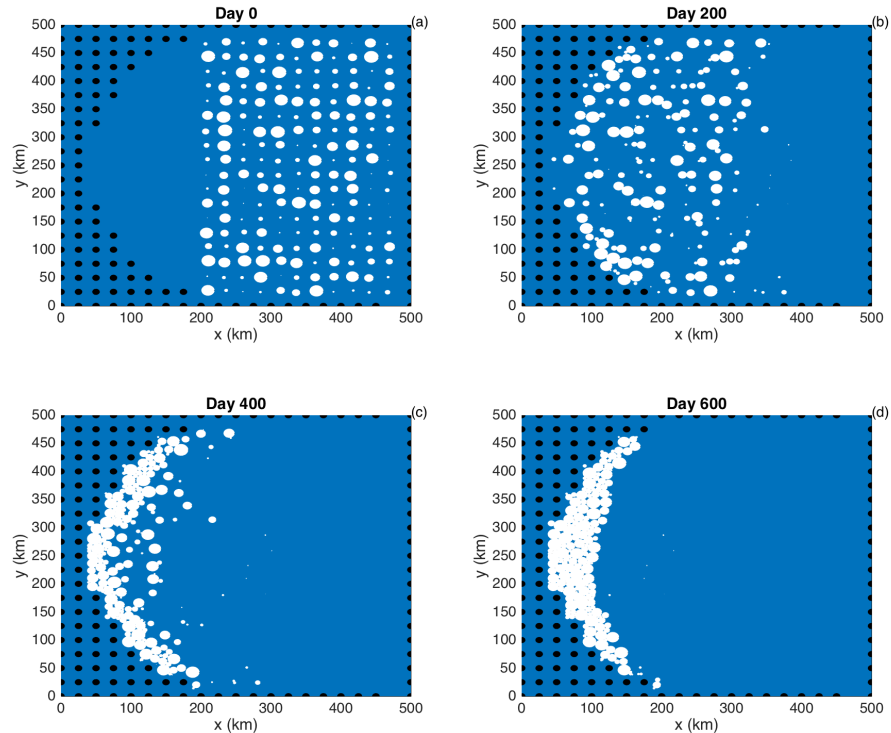


840 **Figure 2.** Snapshots of the fraction of ice cover in the LTIM tabular iceberg calving simulation. Snapshots
 841 are taken (a) 7, (b) 15, and (c) 30 days after calving. The dashed line in panel (c) shows the location of the
 842 vertical transects shown in Figures 8 and 8.

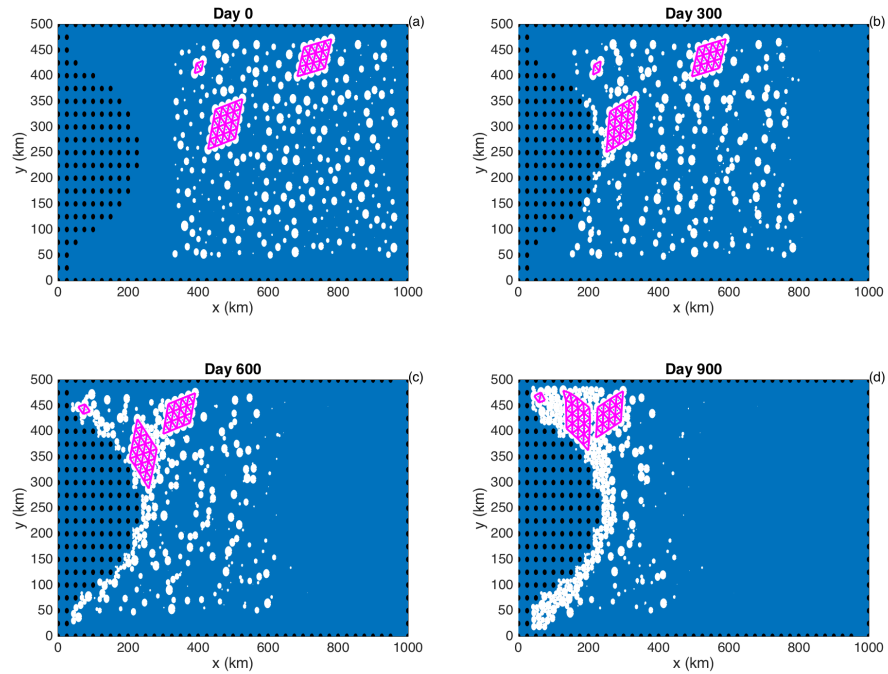
833 (a) Hexagonal elements are initialized in a staggered lattice as shown. Adjacent ele-
 834 ments are bonded together. The element bonds (plotted in pink) form equilateral triangles
 835 which give the larger structure rigidity. The black circles show the circular element shape
 836 used in element interactions, and are inscribed inside the hexagonal shape used for mass-
 837 spreading. (b) Intersection of a hexagonal element and the ocean grid. The colors indicate
 838 the fraction of the hexagon that lies in each grid cell. These fractions are used as weights
 839 to spread LTIM properties to the ocean grid (see text for more details).



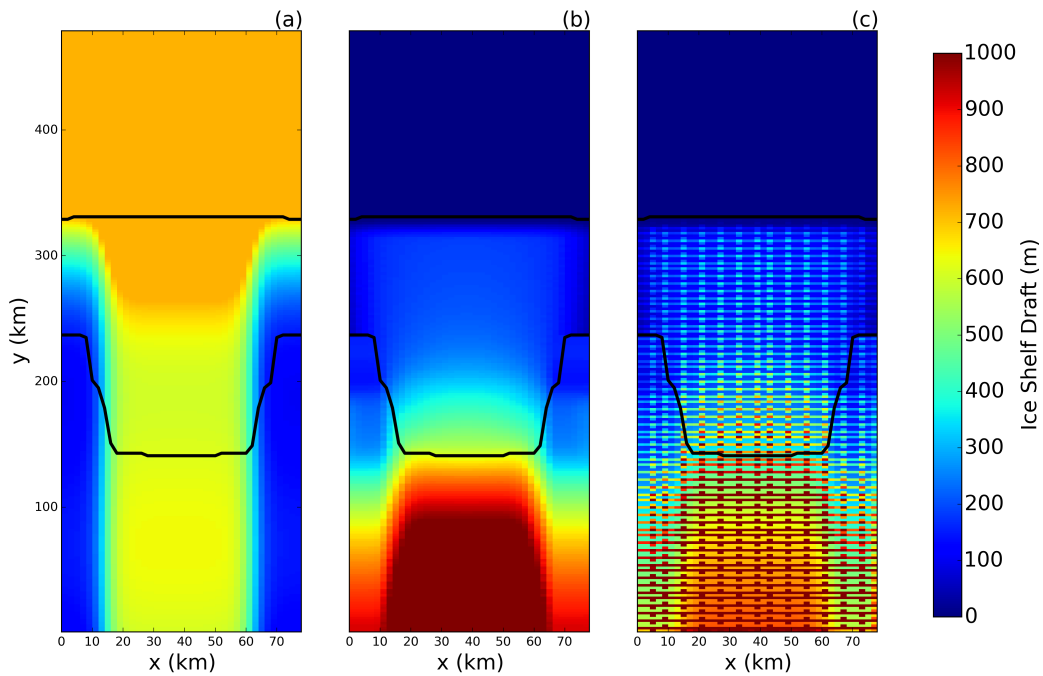
843 **Figure 3.** Snapshots of the sea surface temperature in the LTIM tabular iceberg calving simulation. Snap-
844 shots are taken (a) 7, (b) 15, and (c) 30 days after calving. Regions with ice area fraction = 1 area plotted in
845 white.



846 **Figure 4.** Results of an ice-only LTIM simulation with no bonds between ice elements. Ice elements are
 847 initialized throughout the domain, as shown in panel (a). The elements are forced by an imposed westward
 848 ocean current of $u=0.1\text{m/s}$ (no ocean model is used). Forces due to sea surface slope, atmospheric drag, Cori-
 849 olis and sea ice drag are set to zero. The figure shows snapshots of ice element positions at time (a) $t=0$, (b)
 850 (c) 400, (d) 600 days. The size of the dots shows the surface area (and interaction diameter) of each ice
 851 element. Land points are shown by black circles.



852 **Figure 5.** Results of an ice-only LTIM simulation using bonds between elements. Ice elements are initial-
 853 ized throughout the domain, as shown in panel (a). Three tabular icebergs are included, with 25, 16 and 4
 854 elements respectively. The elements are forced by an imposed westward ocean current of $u=0.1\text{m/s}$ (no ocean
 855 model is used). Forces due to sea surface slope, atmospheric drag, Coriolis and sea ice drag are set to zero.
 856 The figure shows snapshots of ice element positions at time (a) $t=0$, (b) 300, (c) 600, (d) 900 days. The size
 857 of the dots shows the surface area (and interaction diameter) of each ice element. Bonds between ice elements
 858 are plotted in magenta. Land points are shown by black circles.



859 **Figure 6.** (a) Ocean bottom topography and (b) ice-shelf draft used to initialized the tabular iceberg calv-
860 ing simulation. The ice draft is calculated from the total mass in an ocean grid cell after the mass-spreading
861 interpolation has been applied (as explained in Section 2.3). (c) Initial ice draft that would be calculated if the
862 mass-spreading interpolation were not used (i.e.: elements treated as point masses).

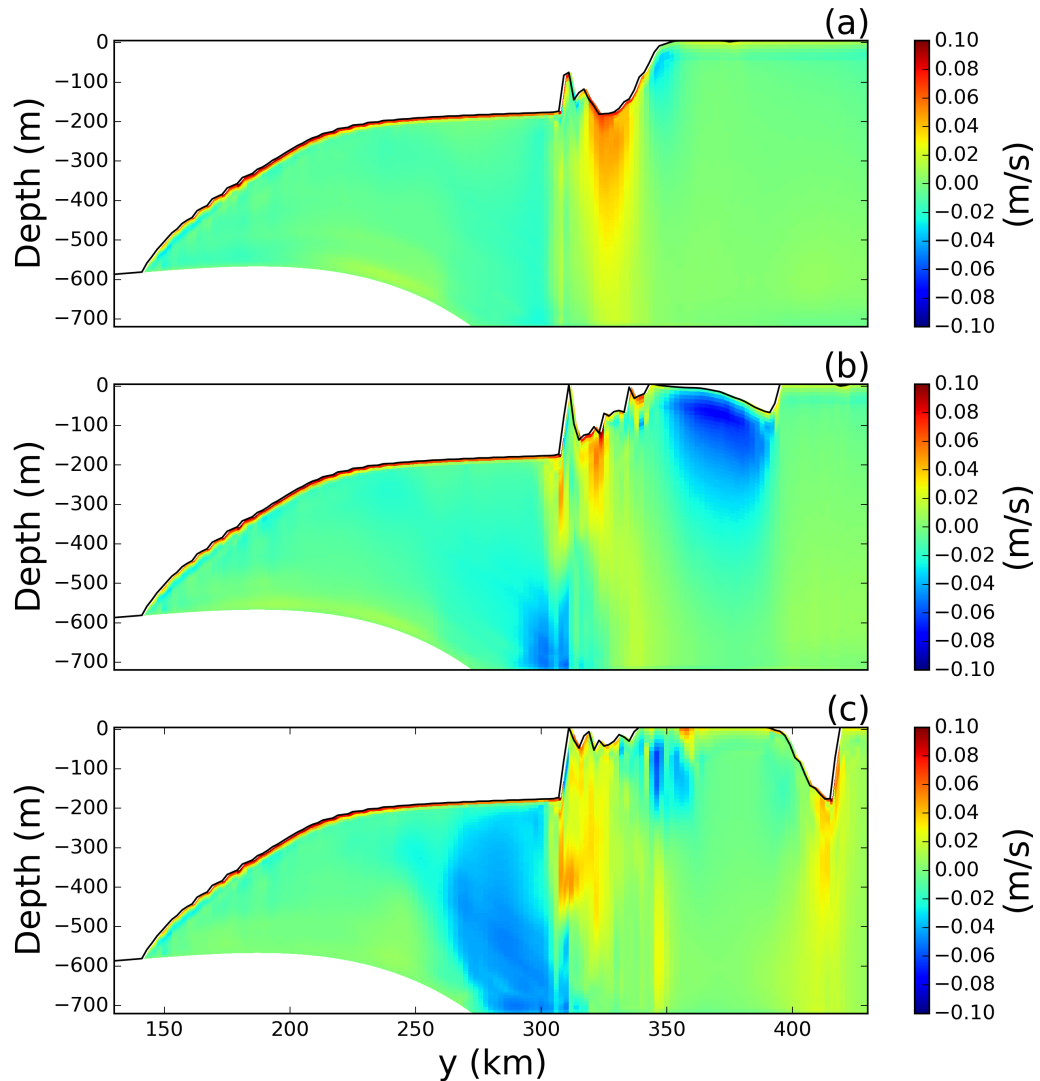


Figure 7. Snapshots of vertical sections of meridional velocity at $x = 58\text{ km}$ in the LTIM tabular iceberg calving simulation. Snapshots are taken (a) 7, (b) 15, and (c) 30 days after calving. The position of the transects is shown by the dashed line in Figure 8c.

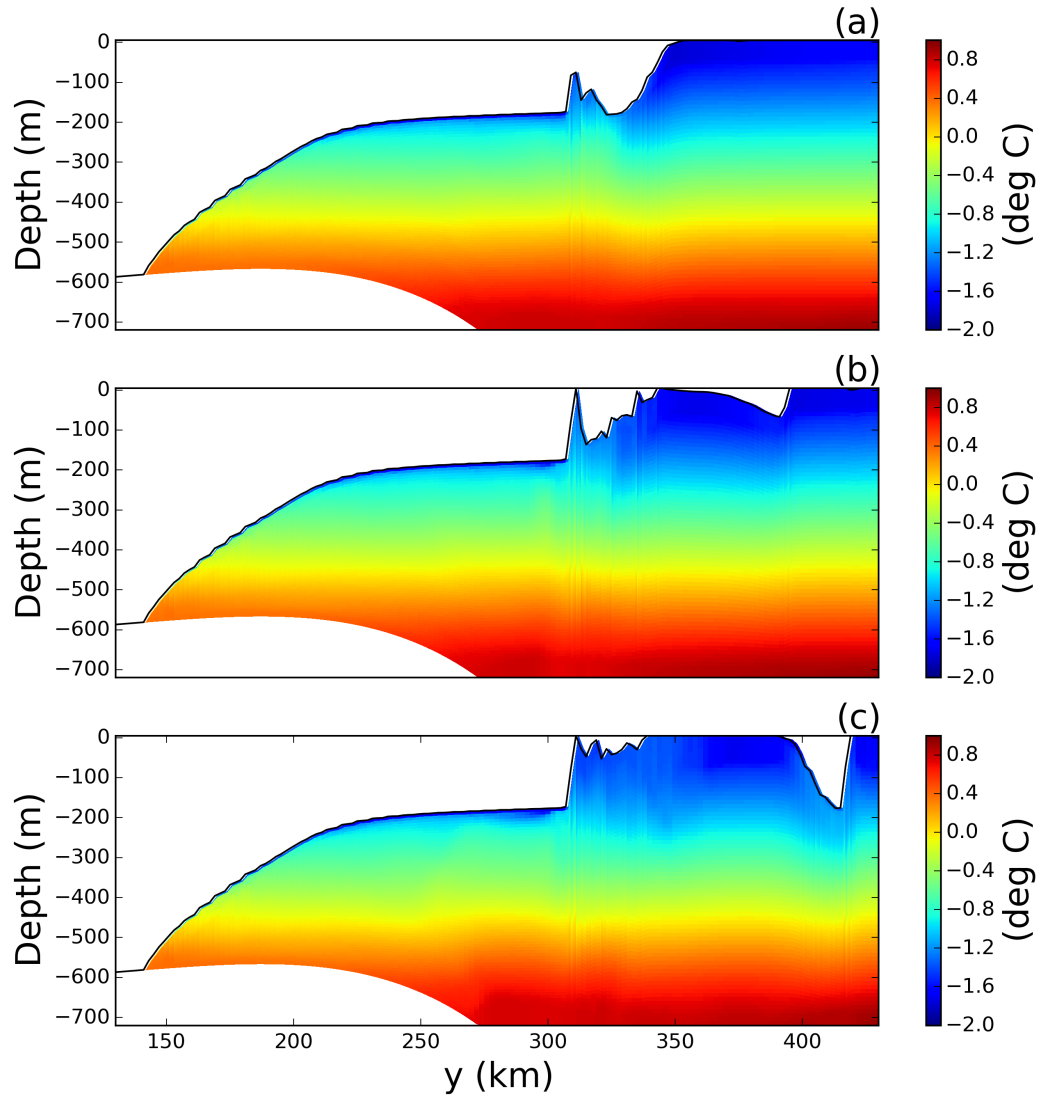
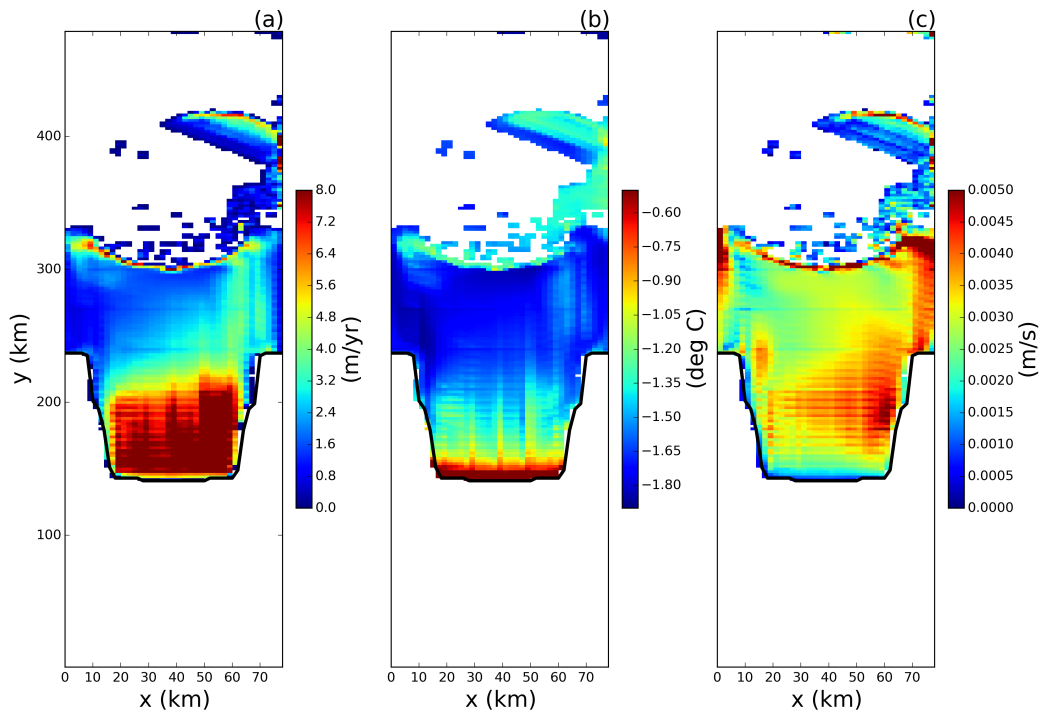
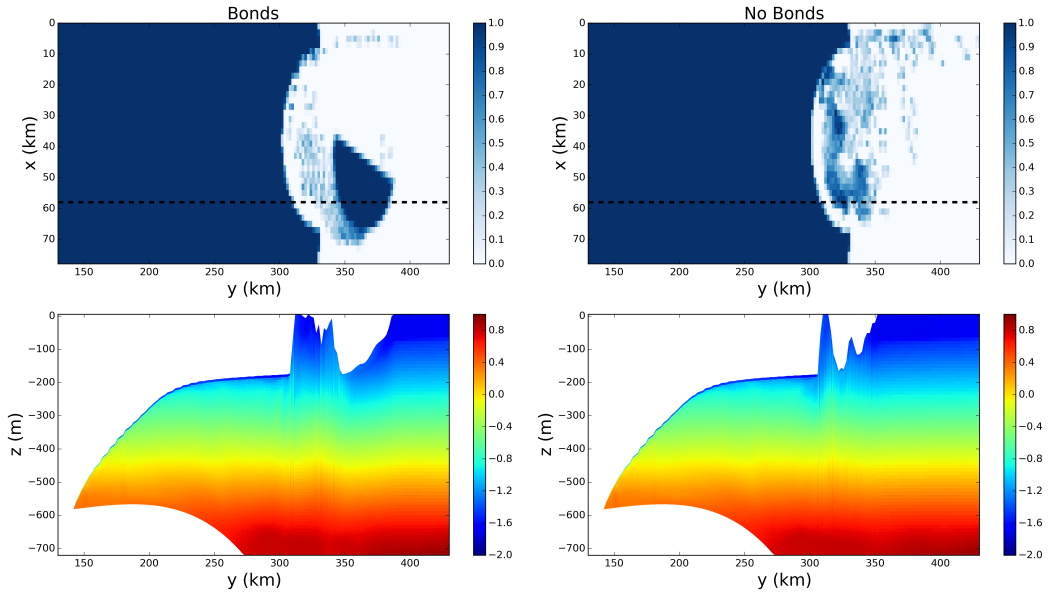


Figure 8. Snapshots of vertical sections of ocean temperature at $x = 58\text{ km}$ in the LTIM tabular iceberg calving experiment. Snapshots are taken (a) 7, (b) 15, and (c) 30 days after calving. The position of the vertical transects is shown by the dashed lines in Figure 8c.



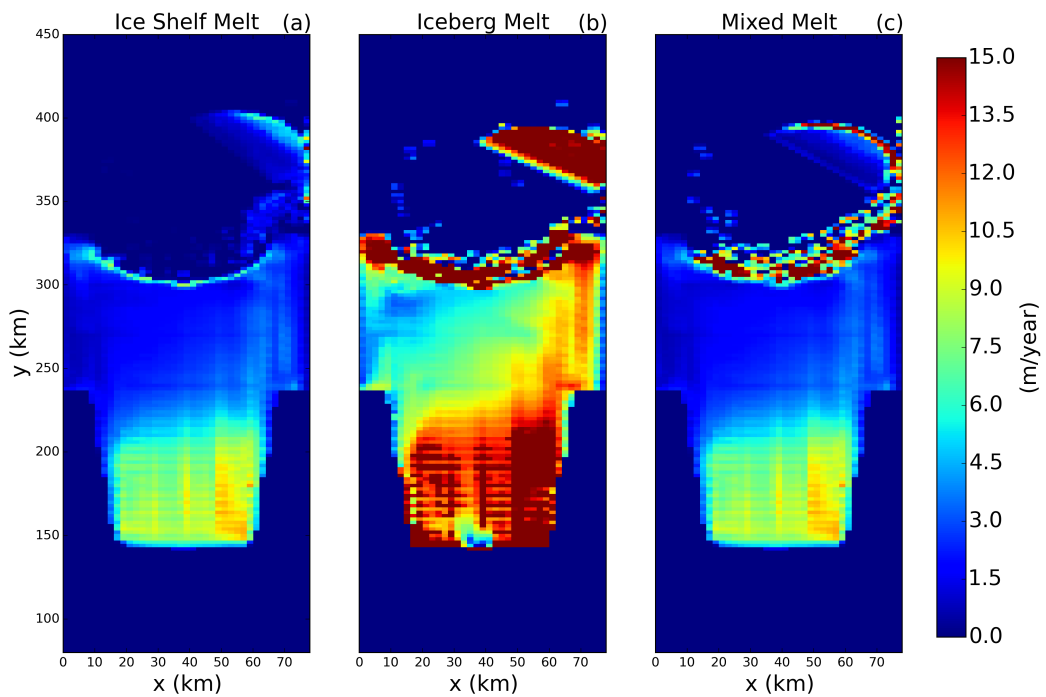
869 **Figure 9.** Results of the tabular iceberg calving simulation 30 days after the iceberg calves. The three panels
870 show snapshots of the (a) melt rate, (b) top-of-ocean temperature and (c) u^* at the base of the ice shelf.
871 Fields are only shown in regions where the ice area fraction is ≥ 0.8 .



872 **Figure 10.** Results from the tabular iceberg calving experiment with and without iceberg bonds. The top
 873 row shows the fractional ice cover for the simulations (a) with and (b) without numerical bonds. The bottom
 874 row shows the corresponding vertical temperature section at $x = 58\text{ km}$ for the simulation (c) with and (d)
 875 without bonds. The location of the vertical transects in panels (c) and (d) are shown by the dashed lines in
 876 panels (a) and (b), respectively. All snapshots are taken at time $t = 30$ days. The simulations use wind stress
 877 $\vec{\tau} = <0.0, 0.05>$.

878

9 Extra Figure:



879 **Figure 11.** Melt rate 30 days after calving for simulations using (a) three equation
880 model, (b) icebergs drift parametrization, (c) a mixture between the two (as described in Section 2.5.)

881 **10 Supplementary Material**

882 The experiment configuration used to initialize the calving tabular iceberg simulation
883 (in this study) is the same as that of the Ocean0 setup in the MISOMIP, with the follow-
884 ing three changes made:

- 885 1. The ‘calving criteria’ used in the MISOMIP study (which states that all points in
886 the ice shelf with thickness less than 100m are set to zero thickness) has not been
887 used.
- 888 2. The ice shelf has been thickened on the flanks of the domain, so that the latitude of
889 the grounding line increases away from the center of the ice shelf.
- 890 3. The ice shelf is configured to be symmetric about its meridional center line ($x =$
891 $\frac{L_x}{2}$). This was achieved by using the average of the left and right flanks of the ice-
892 shelf thickness.

893 These three changes were made in order to make the circulation beneath the ice shelf eas-
894 ier to interpret.